JOURNAL OF GUIDANCE, CONTROL, AND DYNAMICS
Vol. 27, No. 6, November–December 2004

Retargeting Dynamics of a Linear Tethered Interferometer

Claudio Bombardelli*
University of Padova, Padova 35131, Italy
Enrico C. Lorenzini†
Harvard–Smithsonian Center for Astrophysics, Cambridge, Massachusetts 02138
and
Marco B. Quadrelli‡
Jet Propulsion Laboratory, California Institute of Technology, Pasadena, California 91109

The study deals with the issue of changing the plane of rotation (retargeting) of a linear kilometer-sized formation of two collectors and one combiner spacecraft connected by two tether arms. A control strategy is proposed that makes use of a pair of electrical thrusters located onboard two of the three spacecraft to redirect the angular momentum of the formation to a new target with an accuracy of a few arcseconds while keeping the angular momentum magnitude constant throughout the maneuver. The thruster profile is optimized to achieve a very smooth but relatively fast maneuver while maintaining the overall fuel consumption at a minimum level. The attitude dynamics of the formation are solved analytically based on a perturbation method, which allows calibrating the thrust profile for high-precision retargeting. A numerical model is employed to test the proposed strategy and to evaluate the influence of massive flexible tethers and external perturbations on the accuracy of the maneuver. Finally, the required propellant mass is evaluated with reference to envisioned space interferometry missions.

Introduction

PRECISION retargeting of long-baseline formations in space, both free-flying and structurally connected, is a key aspect of many future space-borne interferometry missions.

First, the maneuver has to be performed with very high precision to keep the optical path delay (OPD) between the apertures small enough to be effectively compensated for by optical delay lines onboard the combiner unit. Delay lines envisioned for future space interferometers have a total stroke on the order of 10 cm, resulting in a required pointing precision of about 20 in. when the interferometer baseline reaches kilometer size. Second, the time spent for the maneuver has to be kept to a minimum, because no scientific observation can be carried on during the maneuver. Third, the propellant needed (for direct slewing or reaction-wheel desaturation) should be minimized to save launch costs and most of all to avoid aperture and thermal shield contamination by thruster plumes.[1] Last, the maneuver should be designed with the required smoothness in order to prevent the buildup of broadband vibrations that can saturate the optical-path-delay control actuators. All these aspects are considered in the present analysis.

The idea of using tether technology for interferometry purposes was already explored in the late 1960s and early 1970s (Refs. 2–4) through the use of gravity-gradient-stabilized systems. Later, in the 1980s, Crellin[5] and Decou[6] proposed a concept of a three-body spinning interferometer (Trio) that could be pointed at different inertial targets. For the case of a tethered interferometer with linear configuration the pointing stability of the formation during acquisition mode was investigated by Bombardelli et al.,[7] who provided a method of relating the optical path delay of the interferometer to the dynamics of the system. Although existing environmental perturbations were examined, retargeting of the formation was not addressed.

A description of a retargeting strategy for a two-dimensional formation is given by Farley and Quinn,[8] who proposed the use of thrusters located at the subapertures to precess the formation while it spun. Farley and Quinn[8] show how the propellant consumption can be minimized by performing the maneuver when the subapertures are the farthest away from the center of rotation of the system.

This paper analyzes the maneuver in detail and proposes a novel retargeting strategy suited for one-dimensional formations, which allows high-precision pointing in a relatively short maneuver time. The thrust direction during the maneuver is kept constantly orthogonal to the tether axis and to the direction of the instantaneous velocity of each collector, with the advantages of avoiding stretching the tethers and leaving the interferometer angular rate unchanged. Furthermore, the thrust profile is shaped as a squared sine function with zero derivatives at the edges in order to limit the buildup of lateral oscillations at the end of each maneuver.

The pointing dynamics of the formation during the slewing process are investigated in three steps:

1) The retargeting dynamics of a rigid dumbbell model for the formation are solved analytically. We write the equations of motion of the formation angular velocity in body axes and solve the attitude kinematic equations with the aid of an asymptotic expansion for a set of Euler angles. Knowing the Euler angles at the end of the maneuver as a function of the thrust magnitude allows the calibration of the thrust profile for precision retargeting.

2) The retargeting dynamics of a model composed of three point masses connected by two flexible viscoelastic tether arms are solved numerically with a high-fidelity lumped-mass model. The model includes the effect of environmental perturbations acting while the maneuver is being carried out. Tether thermal effects are also taken into account.

3) The results from the two models are compared to assess how the dynamics of the flexible tethers, the environmental perturbations, and the presence of a third body in the middle of the configuration influence the accuracy of the proposed maneuver.

Finally, the propellant consumption to change the angular momentum of the formation is computed with reference to envisioned space interferometry missions.

Presented as Paper 2003-0222 at the AAS/AIAA 13th Spaceflight Mechanics Meeting, Ponce, PR, 9–13 February 2003; received 6 June 2003; revision received 15 April 2004; accepted for publication 10 May 2004.

*Ph.D. Candidate, Faculty of Engineering, Centro Interdipartimentale Studi e Attivitá Spaziali; also Visiting Student, Harvard–Smithsonian Center for Astrophysics, Cambridge, MA 02138.

†Staff Scientist, Radio and Geoastronomy Division. Senior Member AIAA.

‡Staff Member, Guidance and Control Section.

Optical Path Delay Stability

One of the most important parameters to be taken into account when dealing with an interferometric system is the OPD between each pair of subapertures (collectors) with respect to a central combining unit (combiner).

The OPD is defined as the pathlength difference that the light from the observed source experiences in reaching the combining unit detector following two different paths: one through the first collecting aperture and one through the second (Fig. 1).

The OPD depends not only on the relative positions of combiner and collectors with respect to the target source but also on the relative motion of optical components onboard each single unit induced by structural vibrations (e.g., due to reaction-wheel disturbances) and thermal loads.

To obtain a meaningful interferometric signal the rms of the OPD must be limited to a value ranging from a fraction of a wavelength to a few wavelengths, depending on the type of measurement. For this reason, the combining unit is equipped with a series of actuators (delay lines) properly controlled to keep the OPD below a prescribed value. Given the spectrum of the overall OPD disturbances, the delay-lines control loop may or may not be able to accomplish the stabilization task.

In the present analysis we are interested in the part of the OPD disturbances related to the motion of the three spacecraft, modeled as point masses under the influence of the dynamics of the tethers connecting them, the environmental perturbations, and the thruster forces during a retargeting maneuver.

Following the scheme of Fig. 2, the OPD can be seen as a sum of two components. The first is the difference $l_2 - l_1$ between the distances of the two collectors to the combiner. For the case of a tethered interferometer this component is influenced by the tethers' longitudinal dynamics and low-frequency differential thermal elongation. The second OPD component $(z_2 - z_1)$ comes from the fact that in general the ideal line joining the two apertures (baseline) is not orthogonal to the source direction $\boldsymbol{Z}$. This is due to the action of external perturbations, the tethers' lateral dynamics, and mispointing of the average aperture rotation plane with respect to the target.

Bombardelli et al.[7] show how the latter component of the OPD disturbance is determined by the direction of the angular momentum $\boldsymbol{L}$ of the system collector1 + collector2, seen as point masses, with respect to its barycenter. We will refer to $\boldsymbol{L}$ as the baseline pointing vector of the formation. On the basis of this definition one can write

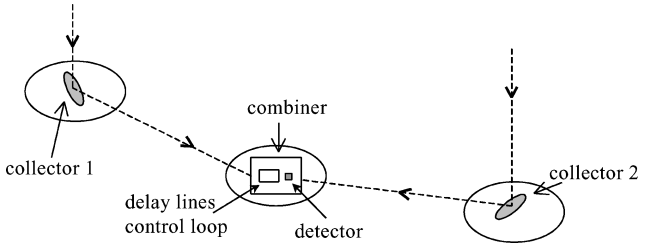

Fig. 1 Schematic of interferometric OPD.

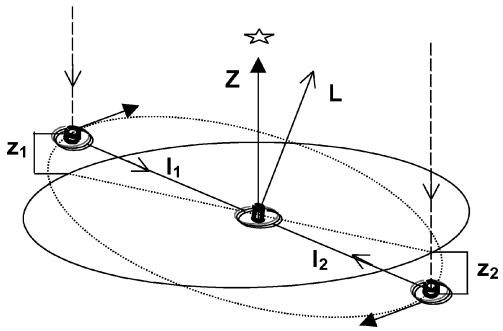

Fig. 2 OPD arising from an offset between the apertures' angular momentum and the source direction.

the equations of motion for $\boldsymbol{L}$ under the effect of the external torques $\boldsymbol{M}_{\text{ext}}$, taking into account that the overall system angular momentum also includes the tethers' angular momentum $\boldsymbol{L}_{\text{teth}}$ and the central combiner angular momentum $\boldsymbol{L}_{\text{cmb}}$:

$$\boldsymbol{L}(t) = \int_0^t \boldsymbol{M}_{\text{ext}}\,\mathrm{d}t - \boldsymbol{L}_{\text{teth}}(t) - \boldsymbol{L}_{\text{cmb}}(t) \tag{1}$$

The important consequence of Eq. (1) is that even in the absence of external torques the baseline pointing dynamics (and therefore the OPD) are perturbed by the tethers' lateral dynamics through an exchange of angular momentum between tethers and collecting apertures at the tethers' attachment points. Because a retargeting thrusting maneuver can potentially excite the tethers' lateral dynamics and give rise to angular momentum fluctuations between tethers and collecting apertures, it is important to design it with the required smoothness.

All in all, in an attempt to reduce the disturbances to be compensated for by the OPD control loop, the retargeting algorithm has to bring the baseline pointing vector as close as possible to the prescribed target with the smallest amount of residual tether oscillation, thereby reducing the maximum stroke and bandwidth required by the control actuators.

Retargeting Strategy

The proposed retargeting strategy has the following characteristics:

1) The thrust, provided by a high-precision propulsion system located on two of the three platforms, is applied along a direction always normal to the instantaneous rotation plane of the spinning interferometer.

2) The thrust-time profile covers a portion of the overall rotation period of the interferometer and is shaped as a sine-square function in order to keep the tether lateral oscillations to a minimum (Fig. 3).

Directing the thrust as in characteristic 1 has the major advantage of maintaining a constant modulus of the angular momentum and therefore holding the angular rate of the formation at a constant value without applying any additional tension along the tethers.

With regard to the position and orientation of the thrusters on the platforms, two schemes are envisioned, as shown in Fig. 4. Scheme b has the advantage of keeping the thruster exhaust away from the

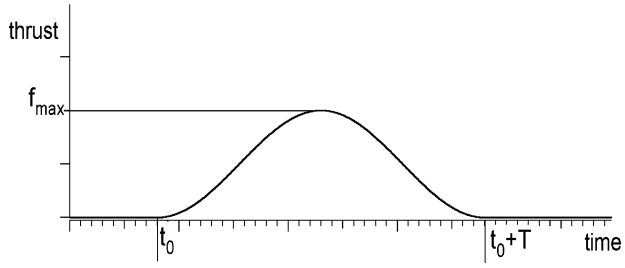

Fig. 3 Retargeting thrust profile.

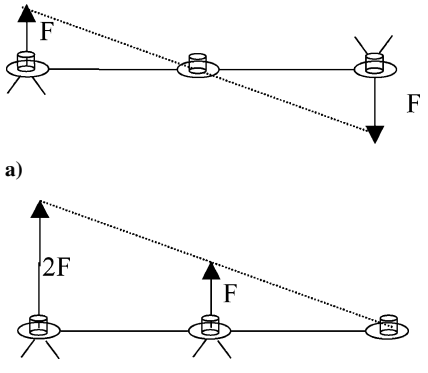

Fig. 4 Possible thruster firing schemes.

optics at the price of greater fuel expenditure and greater thrust. By switching the platform subjected to greater thrust for each retargeting maneuver it is possible to equalize the mass variation throughout the mission and in turn to limit the buildup of unbalanced solar-radiation torques. As far as the attitude dynamics of the formation is concerned, the two cases are very similar, and the following analysis can be applied to both with few adjustments.

Precision Retargeting

Let us consider a spinning dumbbell system (modeled as two equal point masses connected by a massless rigid rod) whose angular momentum is initially pointed at the target A. Let the dumbbell length be $2R$ and its initial spin rate ω. Let (X, Y, Z) be an inertial reference frame having Z oriented toward A, X lying along the dumbbell axis at $t=0$, and (x, y, z) a body frame with x lying along the dumbbell axis and z oriented as the dumbbell angular momentum. Let ψ_f and ν_f be the precession and nutation angles by which the body frame has to be rotated according to a 3–1–3 Euler sequence so that the dumbbell angular momentum overlaps with a destination target $\boldsymbol{B}$, as shown in Fig. 5.

The objective of the analysis is to derive the thrust profile for each collector (the scheme of Fig. 3a is considered) whose analytical expression is

$$F_{\text{th}}(t) = f_{\max} \sin^2[(t - t_0)\pi / T] \qquad t \in [t_0; t_0 + T] \tag{2}$$

so that the destination target can be reached with the required accuracy. This requires estimating the appropriate maximum thrust $f_{\max}$ and the start time t_0 of the maneuver for a given target location (ψ_f, ν_f) and maneuver duration T.

Neglecting all of the external perturbations during the maneuver, the forces acting on each end mass m are the tether tension $\tilde{T}$ and the thrust given by Eq. (2). Hence the equilibrium condition for each end mass m, written in body axes in matrix form, yields

$$\begin{bmatrix} 0 & -\dot{\omega}_z & \dot{\omega}_y \\ \dot{\omega}_z & 0 & -\dot{\omega}_x \\ -\dot{\omega}_y & \dot{\omega}_x & 0 \end{bmatrix} \begin{pmatrix} mR \\ 0 \\ 0 \end{pmatrix} + \begin{bmatrix} -\omega_z^2 - \omega_y^2 & \omega_x\omega_y & \omega_x\omega_z \\ \omega_x\omega_y & -\omega_z^2 - \omega_x^2 & \omega_z\omega_y \\ \omega_x\omega_z & \omega_z\omega_y & -\omega_x^2 - \omega_y^2 \end{bmatrix} \begin{pmatrix} mR \\ 0 \\ 0 \end{pmatrix} = \begin{pmatrix} \tilde{T} \\ 0 \\ F_{\text{th}} \end{pmatrix} \tag{3}$$

Before developing Eq. (3) we must point out that, regardless of the forces acting on m, the y component of the angular velocity projected upon the body axes is zero at all times. In fact, with the z body axis oriented (by definition) as the dumbbell angular momentum and the x axis directed along the baseline allows us to write the relation between angular velocity and angular momentum as follows:

$$\begin{bmatrix} 0 & 0 & 0 \\ 0 & I & 0 \\ 0 & 0 & I \end{bmatrix} \begin{pmatrix} \omega_x \\ \omega_y \\ \omega_z \end{pmatrix} = \begin{pmatrix} 0 \\ 0 \\ L \end{pmatrix} \tag{4}$$

where I is the dumbbell moment of inertia around the y and z axis, L is the modulus of the angular momentum, and the moment of inertia about the x axis (baseline) is assumed to be zero. From Eq. (4) we obtain that

$$\omega_y = 0 \tag{5}$$

Consequently, Eqs. (3) yield

$$-m\omega_z^2 R = \tilde{T} \tag{6a}$$

$$mR\dot{\omega}_z = 0 \tag{6b}$$

$$mR\omega_x\omega_z = F_{\text{th}} \tag{6c}$$

Not surprisingly, Eqs. (6a) and (6b) show that the z component of the angular velocity remains constant during the maneuver (and equal to the initial angular rate ω), as does the tether tension.

From Eqs. (5) and (6) we can finally derive the three components of the angular velocity to insert into the kinematic attitude equations of the system. The three components are

$$\omega_x = F_{\text{th}}/m\omega R \tag{7a}$$

$$\omega_y = 0 \tag{7b}$$

$$\omega_z = \omega \tag{7c}$$

The kinematic attitude equations can now be written based on a 2–1–3 Euler sequence (which, unlike the 3–1–3 sequence, does not have a singularity for the initial orientation of the body axes), with the rotation angles being respectively α_1, α_2, and α_3, to yield[9]

$$\dot{\alpha}_1 = \frac{\sin\alpha_3}{\cos\alpha_2} \frac{F_{\text{th}}(t)}{m\omega R} \tag{8a}$$

$$\dot{\alpha}_2 = \cos\alpha_3 \frac{F_{\text{th}}(t)}{m\omega R} \tag{8b}$$

$$\dot{\alpha}_3 = \frac{\sin\alpha_3 \sin\alpha_2}{\cos\alpha_2} \frac{F_{\text{th}}(t)}{m\omega R} + \omega \tag{8c}$$

Given the highly nonlinear character of Eqs. (8) we choose to approach the problem with a perturbation method.

After substituting the expression for F_{th} given by Eq. (2) and rewriting Eqs. (8) in nondimensional form we obtain

$$\dot{\alpha}_1 = \frac{\sin\alpha_3}{\cos\alpha_2} \varepsilon \sin^2\left(\frac{\pi\tau}{\theta}\right) \tag{9a}$$

$$\dot{\alpha}_2 = \cos\alpha_3 \varepsilon \sin^2\left(\frac{\pi\tau}{\theta}\right) \tag{9b}$$

$$\dot{\alpha}_3 = \frac{\sin\alpha_3 \sin\alpha_2}{\cos\alpha_2} \varepsilon \sin^2\left(\frac{\pi\tau}{\theta}\right) + 1 \tag{9c}$$

where the nondimensional time variable is $\tau = \omega t$ and the parameters θ and ε are defined as

$$\theta = \omega T \tag{10}$$

$$\varepsilon = f_{\max} \big/ m\omega^2 R \tag{11}$$

Note that t_0 was set to zero to simplify the notation with no loss of generality.

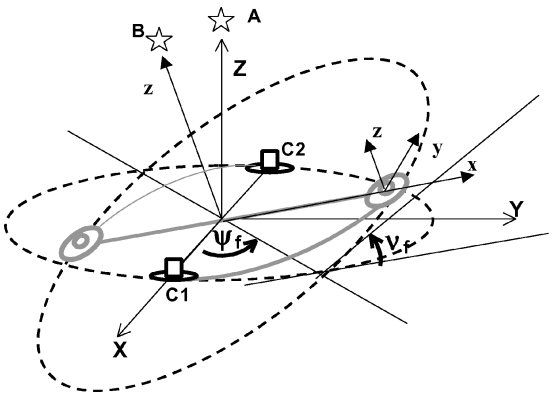

Fig. 5 Collector trajectories during retargeting and reference frames.

It is important to point out the physical meaning of the parameters θ and ε. The former corresponds to the arc length that would be traveled by each end mass for the duration of the maneuver if the masses were to move along an arc of a circle. The latter parameter (as shown in the following) corresponds to the ratio

$$\varepsilon = 2\nu_0/\theta \tag{12}$$

where ν_0 is an approximation of ν_f [see Eq. (21)] obtained by posing

$$\int_0^T F_{\text{th}}(t) R \, \mathrm{d}t = L\nu_0 \tag{13}$$

Equation (12) can be derived by solving the integral in Eq. (13) with $F_{\text{th}}(t)$ expressed as in Eq. (2) and rewriting the expression of the angular momentum as $L = m\omega R^2$ to obtain

$$2\nu_0 = \left(f_{\max}\big/ m\omega^2 R\right)\theta \tag{14}$$

After the definition of ε is taken into account, Eq. (14) leads to Eq. (12).

In other words, as is clear from Eq. (13), ν_0 is the angle by which the angular momentum vector would rotate if its motion induced by the torque $F_{\text{th}}R$ orthogonal to it were to be confined to an inertially fixed plane.

The expansions of α_1, α_2, and α_3 for small ε read

$$\alpha_1(\varepsilon,\tau) = \alpha_{10}(\varepsilon,\tau) + \varepsilon\alpha_{11}(\varepsilon,\tau) + \varepsilon^2\alpha_{12}(\varepsilon,\tau) + \varepsilon^3\alpha_{13}(\varepsilon,\tau) + O(\varepsilon^4) \tag{15a}$$

$$\alpha_2(\varepsilon,\tau) = \alpha_{20}(\varepsilon,\tau) + \varepsilon\alpha_{21}(\varepsilon,\tau) + \varepsilon^2\alpha_{22}(\varepsilon,\tau) + \varepsilon^3\alpha_{23}(\varepsilon,\tau) + O(\varepsilon^4) \tag{15b}$$

$$\alpha_3(\varepsilon,\tau) = \alpha_{30}(\varepsilon,\tau) + \varepsilon\alpha_{31}(\varepsilon,\tau) + \varepsilon^2\alpha_{32}(\varepsilon,\tau) + \varepsilon^3\alpha_{33}(\varepsilon,\tau) + O(\varepsilon^4) \tag{15c}$$

Plugging Eqs. (15) into Eqs. (9) and expanding in Taylor series for small ε yields

$$\begin{aligned}
&\dot\alpha_{10} + \varepsilon\left[\dot\alpha_{11} - S^2\left(\frac{\pi\tau}{\theta}\right)\frac{S\alpha_{30}}{C\alpha_{20}}\right] \\
&\quad + \varepsilon^2\left[\dot\alpha_{12} - S^2\left(\frac{\pi\tau}{\theta}\right)\frac{\alpha_{31}C\alpha_{30} + \alpha_{21}S\alpha_{30}\tan\alpha_{20}}{C\alpha_{20}}\right] \\
&\quad + \varepsilon^3\left\{\dot\alpha_{13} - S^2\left(\frac{\pi\tau}{\theta}\right)\frac{1}{C\alpha_{20}}\left[\alpha_{32}C\alpha_{30} - \frac{\alpha_{31}^2}{2}S\alpha_{30}\right.\right. \\
&\quad + \frac{S\alpha_{30}}{C\alpha_{20}}\left(\frac{\alpha_{21}^2}{2}C\alpha_{20} + \alpha_{32}S\alpha_{20}\right) + \frac{\alpha_{21}S\alpha_{20}}{C^2\alpha_{20}}(\alpha_{31}C\alpha_{20}C\alpha_{30} \\
&\quad \left.\left. + \alpha_{21}S\alpha_{20}S\alpha_{30})\right]\right\} + O(\varepsilon^4) = 0
\end{aligned} \tag{16a}$$

$$\begin{aligned}
&\dot\alpha_{20} + \varepsilon\left[\dot\alpha_{21} - S^2\left(\frac{\pi\tau}{\theta}\right)C\alpha_{30}\right] + \varepsilon^2\left[\dot\alpha_{22} + S^2\left(\frac{\pi\tau}{\theta}\right)\alpha_{31}S\alpha_{30}\right] \\
&\quad + \varepsilon^3\left[\dot\alpha_{23} + S^2\left(\frac{\pi\tau}{\theta}\right)\left(\frac{\alpha_{31}^2}{2}C\alpha_{30} + \alpha_{32}S\alpha_{30}\right)\right] + O(\varepsilon^4) = 0
\end{aligned} \tag{16b}$$

$$\begin{aligned}
&\dot\alpha_{30} - 1 + \varepsilon\left[\dot\alpha_{31} - S^2\left(\frac{\pi\tau}{\theta}\right)S\alpha_{30}\tan\alpha_{20}\right] \\
&\quad + \varepsilon^2\left\{\dot\alpha_{32} - S^2\left(\frac{\pi\tau}{\theta}\right)[\alpha_{21}(S\alpha_{30}S\alpha_{20}\tan\alpha_{20} + S\alpha_{30}C\alpha_{20}) \right. \\
&\quad \left. + \alpha_{31}S\alpha_{20}C\alpha_{30}]\right\} + \varepsilon^3\left\{\dot\alpha_{33} - S^2\left(\frac{\pi\tau}{\theta}\right)\frac{1}{C\alpha_{20}}\right. \\
&\quad \times\left[\alpha_{21}\alpha_{31}C\alpha_{20}C\alpha_{30} + S\alpha_{30}\left(\alpha_{22}C\alpha_{20} - \frac{\alpha_{21}^2}{2}S\alpha_{20}\right)\right. \\
&\quad + S\alpha_{20}\left(\alpha_{32}C\alpha_{30} - \frac{\alpha_{31}^2}{2}S\alpha_{30}\right) \\
&\quad + \frac{S\alpha_{20}S\alpha_{30}}{C\alpha_{20}}\left(\frac{\alpha_{21}^2}{2}C\alpha_{20} + \alpha_{22}S\alpha_{20}\right) \\
&\quad + \frac{\alpha_{21}S\alpha_{20}}{C^2\alpha_{20}}\big(\alpha_{31}S\alpha_{20}C\alpha_{20}C\alpha_{30} \\
&\quad \left.\left.\left. + \alpha_{21}S^2\alpha_{20}S\alpha_{30} + \alpha_{21}C^2\alpha_{20}S\alpha_{30}\big)\right]\right\} + O(\varepsilon^4) = 0
\end{aligned} \tag{16c}$$

where S stands for sine and C for cosine.

An exact solution up to the third order was obtained analytically with the help of symbolic manipulation software. For the sake of brevity the third-order solution is not reported here. In the following we focus on the second-order solution and calibrate the thrust profile on that basis.

By solving the equations in cascade until the second order and with zero initial conditions we obtain

$$\alpha_{10}(\tau) = 0 \tag{17a}$$

$$\alpha_{20}(\tau) = 0 \tag{17b}$$

$$\alpha_{30}(\tau) = \tau \tag{17c}$$

$$\begin{aligned}
\alpha_{11}(\tau) = {}& [1/4(4\pi^2 - \theta^2)]\big\{\theta^2[C(k_2\tau) + C(k_1\tau) - 2C(\tau)] \\
& + 2\pi\theta\cdot[C(k_2\tau) - C(k_1\tau)] + 8\pi^2[C(\tau) - 1]\big\}
\end{aligned} \tag{17d}$$

$$\begin{aligned}
\alpha_{21}(\tau) = {}& [1/4(4\pi^2 - \theta^2)]\big\{\theta^2[-S(k_2\tau) - S(k_1\tau) + 2S(\tau)] \\
& + 2\pi\theta\cdot[-S(k_2\tau) + S(k_1\tau)] - 8\pi^2 S(\tau)\big\}
\end{aligned} \tag{17e}$$

$$\alpha_{31}(\tau) = 0 \tag{17f}$$

$$\alpha_{12}(\tau) = 0 \tag{17g}$$

$$\alpha_{22}(\tau) = 0 \tag{17h}$$

$$\begin{aligned}
\alpha_{32}(\tau) = {}& [1/64\pi(4\pi^2 - \theta^2)^2]\big\{\theta^5[S(2k_5\tau) - 8S(k_5\tau)] \\
& + \pi\theta^4[4S(k_4\tau) + 4S(k_4\tau) - S(k_2\tau) - S(k_1\tau) - 6S(2\tau) \\
& + 12\tau] + \pi^2\theta^3[-4S(k_5\tau) + 48S(k_5\tau) + 8S(k_4\tau) - 8S(k_3\tau) \\
& - 4S(k_2\tau) + 4S(k_1\tau)] + \pi^3\theta^2[-16S(k_4\tau) - 16S(k_3\tau) \\
& - 4S(k_2\tau) - 4S(k_1\tau) + 40S(2\tau) - 80\tau] + \pi^4\theta[-64S(k_5\tau) \\
& - 32S(k_4\tau) + 32S(k_3\tau)] + \pi^5[-64S(2\tau) + 128\tau]\big\}
\end{aligned} \tag{17i}$$

where

$$k_1 = (\theta + 2\pi)/\theta \tag{18a}$$

$$k_2 = (\theta - 2\pi)/\theta \tag{18b}$$

$$k_3 = (\theta + \pi)/\theta \tag{18c}$$

$$k_4 = (\theta - \pi)/\theta \tag{18d}$$

$$k_5 = 2\pi/\theta \tag{18e}$$

We must stress that the choice of a squared sine function for the thrust profile is key to obtaining exact solutions for different orders, as it renders the integrals solvable analytically.

Knowing the angles α_1 and α_2 allows the computation of the corresponding nutation and precession angles. This can be done by

simply writing the inertial components of the angular momentum unit vector both in terms of α_1, α_2 (through the 2–1–3 transformation) and in terms of ψ, ν (through the 3–1–3 transformation)[9]:

$$\boldsymbol{u}_z(\tau) = \{\cos[\alpha_2(\tau)]\sin[\alpha_1(\tau)] - \sin[\alpha_2(\tau)], \cos[\alpha_1(\tau)]\cos[\alpha_2(\tau)]\}^T \tag{19a}$$

$$\boldsymbol{u}_z(\tau) = \{\sin[\nu(\tau)]\sin[\psi(\tau)] - \sin[\nu(\tau)]\cos[\psi(\tau)]\cos[\nu(\tau)]\}^T \tag{19b}$$

from which we derive

$$\nu(\tau) = \cos^{-1}\{\cos[\alpha_1(\tau)]\cos[\alpha_2(\tau)]\} \tag{20a}$$

$$\psi(\tau) = \tan^{-1}\left\{\frac{\sin[\alpha_1(\tau)]\cos[\alpha_2(\tau)]}{\sin[\alpha_2(\tau)]}\right\} \tag{20b}$$

Given the desired nutation ν_f the thrust profile is calibrated by satisfying the condition

$$\nu(\theta) = \cos^{-1}\{\cos[\alpha_1(\theta)]\cos[\alpha_2(\theta)]\} = \nu_f \tag{21}$$

which, assuming a second-order approximation for α_1 and α_2, becomes

$$\cos(\nu_f) = \cos\left[\frac{2\pi^2(1-\cos\theta)}{\theta^2 - 4\pi^2}\varepsilon\right]\cos\left(\frac{2\pi^2\sin\theta}{\theta^2 - 4\pi^2}\varepsilon\right) \tag{22}$$

Finally, given the solution $\bar{\varepsilon}(\nu_f, \theta)$ of Eq. (22) and from the definition of ε given by Eq. (12), the value of $f_{\max}$ necessary to reach the target is

$$f_{\max} = m\omega^2 R\bar{\varepsilon}(\nu_f, \theta) \tag{23}$$

A second-order estimate for the precession angle $\psi(\theta)$ throughout the maneuver can also be computed using Eq. (20b) by setting ε equal to $\bar{\varepsilon}(\nu_f, \theta)$.

Once $\psi(\theta)$ is known, one can compute the maneuver start time to reach the target as

$$t_0 = \lfloor \psi_f - \psi(\theta) \rfloor / \omega \tag{24}$$

The accuracy of the maneuver based on the algorithm presented here has been tested by comparing the second- and third-order approximations with the numerical solution of Eqs. (8).

The accuracy of the second-order approximation, although quite good, does not reach (with the exception of small slew angles) the level of a few arcseconds required by a long-baseline space interferometer.

The pointing errors obtained with a third-order approximation are plotted in Fig. 6 for different values of the ν_f and θ angles. As expected, the wider the slew the less accurate the pointing, so that for slew angles bigger than 10 deg it may be best to perform a series of smaller maneuvers rather than trying to reach the target in a single step. This option would also have the considerable advantage of decreasing the maximum thrust requirements on the propulsion system. On the other hand, it seems reasonable to think that the observing strategy of any space interferometry mission will favor small-angle maneuvers, with the advantage of substantial fuel saving. As far as the maneuver duration is concerned, the accuracy is negligibly affected by the value of θ until it exceeds the 60–70-deg value, where the nutation and precession errors begin to grow.

Figure 7 shows the evolution of the nutation and precession angles (whose accuracies are plotted in Fig. 6) for different thrust durations for an interferometer spinning at one revolution per 67 mm. The plots were obtained by running the tether lumped-mass simulation code and employing the thrust calibration strategy discussed previously.

To completely assess the precision of a retargeting maneuver one has to compute the maximum OPD variation caused by a given error in the nutation and precession angles. After precession and nutation $(\psi_f + \Delta\psi, \nu_f + \Delta\nu)$ according to Eq. (19b), the pointing direction vector yields

$$\boldsymbol{u}_z(\theta) = [S(\nu_f + \Delta\nu)S(\psi_f + \Delta\psi), -S(\nu_f + \Delta\nu)C(\psi_f + \Delta\psi), C(\nu_f + \Delta\nu)]^T \tag{25}$$

whereas the direction of the destination target is

$$\hat{\boldsymbol{L}}_{\text{targ}} = [S\nu_f S\psi_f, -S\nu_f C\psi_f, C\nu_f]^T \tag{26}$$

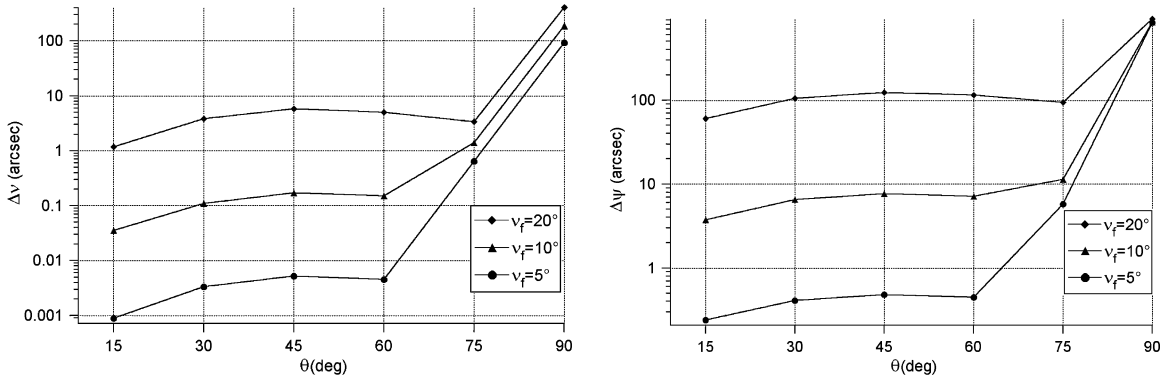

Fig. 6 Dumbbell model nutation and precession errors (arcseconds) after retargeting.

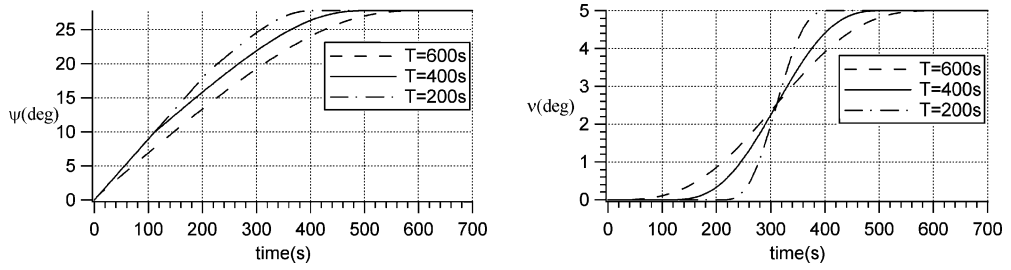

Fig. 7 Nutation–precession curves during retargeting with different thrust durations *T*.

The angle between the two is obtained as

$$\chi = \cos^{-1}\left(\boldsymbol{u}_z^T \hat{\boldsymbol{L}}_{t\text{arg}}\right) = \cos^{-1}\left\{[\cos(\Delta\nu)\cos(\Delta\psi)]\sin^2(\nu_f) + [\sin(\Delta\nu)\cos(\Delta\psi) - \sin(\Delta\nu)]\sin(\nu_f)\cos(\nu_f) + \cos(\Delta\nu)\cos^2(\nu_f)\right\} \quad (27)$$

When $\Delta\psi$ and $\Delta\nu$ are small, χ can be approximated as

$$\chi = \sqrt{\Delta\nu^2 + \Delta\psi^2 \sin^2 \nu_f} \quad (28)$$

and the maximum of the OPD function is simply

$$\text{OPD}_{\text{MAX}} = 2R\sin(\chi) \quad (29)$$

The important conclusion from Eq. (28) is that precession errors have a smaller influence on the OPD than nutation errors, the more so the smaller the slewing angle of the maneuver.

For example, considering a 5-deg slew, an error affecting the precession angle contributes about 10 times less than an error on the nutation angle.

Effect of Flexible Tethers and External Perturbations

The presence of massive flexible tethers will increase the total angular momentum of the system by a very small percentage (the collector/tether mass ratio is about 100:1) and most of all, as explained earlier, will cause angular-momentum fluctuations to rise while the maneuver is being carried out.

The first point can easily be dealt with by adding the estimated angular momentum of the tethers to the overall angular momentum of the system and calculating the thrust profile as in Eq. (23):

$$f_{\max} = m_{\text{eq}}\omega^2 R\bar{\varepsilon}(\nu_f, \theta) \quad (30)$$

where m_{eq} is the equivalent mass representing the total momentum of inertia of the system including tethers.

As far as the angular momentum fluctuations are concerned, they can ideally be brought to zero at the end of the maneuver by tuning the duration of the thrust profile to the tether oscillatory response, as explained in Ref. 10. Lorenzini et al.[10] also propose a very simple strategy to damp out lateral oscillations by means of an internal damping system at the tethers' attachment points. The strong point of this strategy is the fact that it does not cause any drift in the formation pointing because the overall angular momentum of the system is conserved. In fact, after the lateral and longitudinal tether oscillations have been damped out, the system (in its minimum-energy state) will ideally behave as a rigid dumbbell with the OPD variation being attributed only to the initial pointing error and external perturbations.

Several retargeting cases have been run with a high-fidelity lumped-mass numerical model of three 550-kg point-mass platforms interconnected by two 5-kg and 500-m massive flexible tethers spinning at one rotation every 67 mins and flying in an Earth-trailing orbit under the influence of environmental and thermal perturbations. The results were found to differ by less than 5% from the ones obtained with the dumbbell model case (shown in Fig. 6). We can therefore conclude that the accuracy of the retargeting algorithm proposed is not significantly degraded by the presence of the tethers and the external perturbations. We must note that this conclusion is valid as long as the formation is placed in a low-perturbation environment (as is the case in an Earth-trailing heliocentric orbit or a halo orbit around the L2 Lagrangian point) and is spun at a sufficiently high rate to passively counteract the perturbations present in that orbit.[7] Also, the fact of having the combining platform placed at the system center of mass makes its effect on the accuracy of the maneuver negligible. If the combiner is offset from the center of mass then a thrusting action proportional to the platform distance to the system center of mass is needed to properly change its angular momentum.

Propellant Consumption

A tethered interferometer such as the one discussed here in does not require any propellant for formation-keeping during an observation thanks to the constant centripetal acceleration available from the tether tension and to its inherent gyroscopic stability, which keeps the formation pointed without the need of thrust corrections.[7] Consequently the only significant fuel expenditure is that required for slewing the formation and possibly to spin it up or down if a change in angular momentum is required.

Intuitively one would be prone to think that such a high-angular-momentum system (for the system under consideration L can be on the order of 10^6 Nms) would require a great amount of propellant even for only a slew of only a few degrees. On the contrary, the fact of having the thrust applied with a very long lever arm (500 m in this case) from the center of mass of the formation reduces the fuel consumption considerably.

Let β be the desired slew angle and $\boldsymbol{L}$ the angular momentum of each aperture. The overall variation of angular momentum during the maneuver is expressed as

$$\int_0^T R F_{\text{th}}(t)\,\mathrm{d}t = \int_0^T \mathrm{d}\boldsymbol{L} = \frac{L\beta}{\eta_{\text{man}}} = \frac{m\omega R^2\beta}{\eta_{\text{man}}} \quad (31)$$

where $\eta_{\text{man}} < 1$ is the efficiency of the retargeting maneuver and accounts for the fact that L does not follow an arc of a circle (i.e., a pure nutation with zero precession) because of the finite length of the thrust interval. Results from numerical simulations show that η_{man} is greater than 0.95 even for a fairly large thrust interval ($\theta = 90$ deg) and tends to approach unity as the duration of the thrust is decreased.

From Eq. (31) the thrust impulse needed for each slewing maneuver is

$$p = \int_0^T F_{\text{th}}(t)\,\mathrm{d}t = \frac{m\omega\beta R}{\eta_{\text{man}}} \quad (32)$$

which, substituted into the well-known "rocket equation," provides the amount of fuel for each retargeting maneuver as

$$m_{\text{fuel}} = m \times \left[\exp\left(\frac{\omega R\beta}{\eta_{\text{man}} g I_{\text{sp}}}\right) - 1\right] \quad (33)$$

The total propellant mass per spacecraft over the entire mission must take into account the number of targets observed N_t and the average slew angle β_{av} as follows:

$$m_{\text{fuel}}^{\text{tot}} = m \times \left[\exp\left(\frac{\omega R N_t \beta_{\text{av}}}{\eta_{\text{man}} g I_{\text{sp}}}\right) - 1\right] \quad (34)$$

To estimate $m_{\text{fuel}}^{\text{tot}}$ we make the assumption that the average slew angle throughout the mission is 5 deg. This is reasonable if the observation strategy of the mission is optimized. Assuming a mass of 550 kg for the collector and a specific impulse of 1000 s for the thrusters we obtain the plot in Fig. 8.

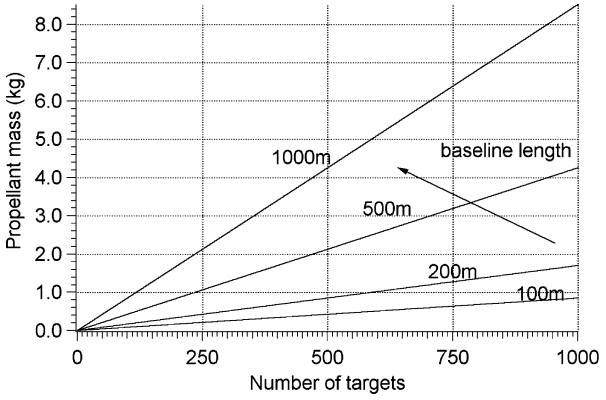

Fig. 8 Total propellant mass vs number of observed targets for different baseline lengths.

For our sample interferometer with two 550-kg collectors each 500 m from the center of rotation and assuming a total of 1000 retargeting maneuvers (over the mission lifetime of 5 years), the total propellant consumption for retargeting is less than 10 kg. In other words, the propellant mass onboard each collector amounts to less than 1% of the total mass of the spacecraft.

Conclusions

An open-loop control strategy has been implemented that allows high-precision retargeting of a kilometer-sized tethered interferometer with one baseline and a linear configuration (i.e., with two collectors and one combiner placed along a line). The maneuver, which employs a pair of thrusters located on two of the three platforms, can be performed rather quickly with high accuracy and extremely low fuel consumption.

Particular attention has been given to the design of a very smooth thrust profile with the result of keeping the tether lateral dynamics at a minimum level.

The pointing accuracy obtainable with the open-loop strategy can reach the level of a few arcseconds for slew angles of less than 10 deg and is not affected significantly by the tether lateral dynamics during the maneuver nor by the external perturbations.

The open-loop profile can form the basis of a feedforward feedback control strategy that compensates for actuator and sensor errors not accounted for in this analysis.

The propellant needed for slewing a kilometer-sized formation spinning at about one revolution per hour is less than 1% of each collector mass for every thousand targets observed and an average slew of 5 deg.

Acknowledgments

The work for this paper was supported by a grant from the Smithsonian Astrophysical Observatory Independent Research and Development program and Contract 1215076 from the Jet Propulsion Laboratory. The authors thank Francesco Angrilli (University of Padova and Centro Interdipartimentale Studi ed Attività Spaziali) for his technical advice and Centro Interdipartimentale Studi ed Attività Spaziali–University of Padova for the support provided to the research activity of C. Bombardelli.

References

[1]Beichman, C. A., Woolf, N. J., and Lindensmith, C. A. (eds.), *Terrestrial Planet Finder*, Jet Propulsion Lab., JPL Publication 99-3, Pasadena, CA, 1999, pp. 115, 116.

[2]Bainum, P. M., Stuiver, W., and Harkness, R. E., "Stability and Deployment Analysis of a Tethered Orbiting Interferometer Satellite System," John Hopkins Univ., Applied Physics Lab., Rept. TG-1045, Silver Spring, MD, Dec. 1968.

[3]Bainum, P. M., Harkness, R. E., and Stuiver, W., "Attitude Stability and Damping of a Tethered Orbiting Interferometer Satellite System," *Journal of the Astronautical Sciences*, Vol. 19, No. 5, 1972, pp. 364–389.

[4]Stuiver, W., and Bainum, P. M., "A Study of Planar Deployment Control and Libration Damping of a Tethered Orbiting Interferometer Satellite," *Journal of the Astronautical Sciences*, Vol. 20, No. 6, 1973, pp. 321–346.

[5]Crellin, E. B., "Preliminary Studies of a Spinning Tether Connected Trio Concept," *Proceedings of the Colloquium on Kilometric Optical Arrays in Space*, edited by N. Longdon and O. Melita, ESA, Paris, 1985, p. 91.

[6]Decou, A. B., "Gravity Gradient Disturbances on Rotating Tethered Systems in Circular Orbit," *Proceedings of the 3rd International Conference on Tethers in Space Toward Flight*, AIAA, Washington, DC, 1989, pp. 343–351.

[7]Bombardelli, C., Lorenzini, E. C., and Quadrelli, M. B., "Formation Pointing Dynamics of Tether-Connected Architecture for Space Interferometry," *Journal of the Astronautical Sciences* (submitted for publication).

[8]Farley, R. E., and Quinn, D. A., "Tethered Formation Configurations: Meeting the Scientific Objectives of Large Aperture and Interferometric Science," AIAA Paper 2001-4770, Aug. 2001.

[9]Hughes, P. C., *Spacecraft Attitude Dynamics*, Wiley, New York, 1986, pp. 18–29.

[10]Lorenzini, E. C., Bombardelli, C., and Quadrelli, M. B., "Analysis and Damping of Lateral Vibrations in a Linear Tethered Interferometer," *Advances in the Astronautical Sciences*, Vol. 114, American Astronautical Society, Springfield, VA, 2003, pp. 1749–1768.